

Effect of shear on coherent structures in turbulent convection

Prafulla P. Shevkar

*Department of Applied Mechanics,
Indian Institute of Technology Madras, Chennai 600036, India*

G. S. Gunasegarane

*Department of Mechanical Engineering,
Pondicherry Engineering College, Pillaichavadi, Puducherry 605014, India*

Sanal K. Mohanan and Baburaj A. Puthenveettil*

*Department of Applied Mechanics,
Indian Institute of Technology Madras, Chennai 600036, India*

(Received 14 January 2019; published 17 April 2019)

We study the effect of shear on the coherent structures near the hot surface, namely, line plumes, in turbulent Rayleigh-Bénard convection (RBC) and turbulent mixed convection (MC) for the range of near-surface Rayleigh numbers $5.75 \times 10^7 \leq Ra_w \leq 2.17 \times 10^9$ and shear Reynolds numbers $8.02 \times 10^2 \leq Re \leq 15 \times 10^3$ for a Prandtl number range of $10.1 \geq Pr \geq 0.7$ in water and air. Plumes are visualized by particle scattering in MC in air while they are extracted from the particle image velocimetry fields in RBC in water. We also use the planforms of plume structure obtained by Gilpin *et al.* [*J. Heat Transfer* **100**, 71 (1978)] in MC in water using electrochemical visualization, as well as those obtained by Pirozzoli *et al.* [*J. Fluid Mech.* **821**, 482 (2017)] in simulations. The planforms of plume structure show that shear aligns the line plumes and increases their mean spacing λ . An increase in Ra_w decreases λ , while the resulting increase in Re in RBC, due to the increase of larger large-scale flow strength, counteracts this effect. Further, plumes are seen more spaced and smeared in air, compared to that in water, due to the lower Pr . We show that these complex dependences of λ on Ra_w , Re , and Pr in RBC and MC can be described by a common scaling law $\lambda^* = \lambda - \lambda_0 = SZ_{sh}/D$, where λ_0 is the mean plume spacing in the absence of shear, $S = Re^3/Ra_w$ is a shear parameter, $Z_{sh} = \nu/U_{sh}$ is the viscous-shear length, and D a function of Pr .

DOI: [10.1103/PhysRevFluids.4.043502](https://doi.org/10.1103/PhysRevFluids.4.043502)**I. INTRODUCTION**

In turbulent Rayleigh-Bénard convection (RBC), line plumes are the predominant coherent structures that originate in the diffusive regions near the hot surface. These line plumes form, merge, and rise, resulting in a complex network of lines on the hot surface, which essentially act as channels transporting heat from the diffusive regions near the plate into the fully turbulent bulk. Since the majority of the heat from the hot plate is transported by these coherent structures [1], understanding the scaling of their geometry is essential in understanding the phenomenology of flux scaling in turbulent convection.

*apbraj@iitm.ac.in

These lines plumes are the outcome of the gravitational instability of the local natural convection boundary layers [2] that form on the hot surface; the spacings between them are then indicative of the length at which these local boundary layers become unstable. In the absence of predominant shear, these spacings are distributed lognormally at any instant [3,4], with λ_0 , the mean plume spacing in the absence of shear, scaling as

$$\lambda_0 = C_1 \text{Pr}^{n_1} Z_w, \quad (1)$$

where $C_1 = 47.5$, $n_1 = 0.1$, and $\text{Pr} = \nu/\alpha$ is the Prandtl number [5], with ν being the kinematic viscosity, α the thermal diffusivity, and the subscript 0 indicating the no-shear values hereinafter. Here

$$Z_w = \left(\frac{\nu\alpha}{g\beta\Delta T_w} \right)^{1/3} = \frac{H}{\text{Ra}_w^{1/3}} \quad (2)$$

is a length scale near the plate [6,7], where the near-surface Rayleigh number $\text{Ra}_w = g\beta\Delta T_w H^3/\nu\alpha$, with β being the coefficient of thermal expansion, H the layer height and ΔT_w the temperature drop between the hot plate and the bulk. The relation (1) also implies that

$$\text{Ra}_{\lambda_0}^{1/3} = C_1 \text{Pr}^{n_1}, \quad (3)$$

where $\text{Ra}_{\lambda_0} = g\beta\Delta T_w \lambda_0^3/\nu\alpha$ is the Rayleigh number based on λ_0 . Since the total length of plumes L_p over an area A of the hot plate is $L_p = A/\lambda_0$, (1) and (2) also imply that

$$\frac{L_p}{A/H} = \frac{\text{Ra}_w^{1/3}}{C_1 \text{Pr}^{n_1}}, \quad (4)$$

as shown by Puthenveetil *et al.* [5]. The same scaling, without the Pr dependence, has also been obtained by Bosbach *et al.* [8], who connected it empirically to the volume-averaged Kolmogorov length.

At higher Ra_w , these line plumes organize themselves to create a large-scale flow, which then change the flux scaling from the classical $\text{Nu} \sim \text{Ra}^{1/3}$ scaling law, where Nu is the Nusselt number and the Rayleigh number $\text{Ra} = 2\text{Ra}_w$. This anomalous flux scaling is expected to be due to the modification of the boundary layers by the shear due to the large-scale flow. The nature of this modification is still not clear, with the popular theory of Grossman and Lohse [9] assuming that the boundary layers become Blasius boundary layers, which, however, has not been previously observed [10,11]. Similar modification of boundary layers due to shear is expected in mixed convection (MC) where the shear is provided by an externally imposed horizontal mean flow. Studies abound on the heat flux scaling in MC, where an empirical summation of the power law scalings in the limiting cases of forced convection and free convection are often used [12–15]. These changes in the flux scaling with shear in RBC and MC, whose phenomenology is still not clear, could also be expected to alter the structure of the line plumes on the hot surface with shear since the heat flux is mostly transported by plumes.

Quantitative knowledge about such changes to the plume structure with shear, in terms of the changes in the spacings between the line plumes, is, however, limited. Various visualizations in RBC [3,16] and MC [13,15,17,18] show that shear aligns the line plumes along the shear direction. In both these cases, it is, however, not known whether shear changes the spacings between these coherent structures, and if it changes, how much that change will be from that given by (1) for the case of no predominant shear. No knowledge of the scaling of the spacings with ΔT_w and the shear velocity U_{sh} , or on the corresponding dimensionless parameters Ra_w and the shear Reynolds numbers $\text{Re} = U_{\text{sh}}H/\nu$ is available. Since these coherent structures carry most of the heat from the hot surface [1], such knowledge about changes in the nature of the plume structure with shear could be crucial in understanding the shear-engendered, anomalous, heat flux scaling in turbulent convection. Such knowledge could also lead to ways to improve the heat transfer from surfaces by manipulating these structures. Further, the geometry, organization, and dynamics of these coherent structures are of

interest in the overall phenomenology of turbulent RBC and MC, like the importance of coherent near wall vortices in shear turbulence [19]. In addition, knowledge about the spacing and the length of these line plumes could also lead to effective wall functions for modeling of turbulent RBC and MC, as has been done in shear turbulence [20,21].

In the present study, we study the effect of shear on the spacing between the coherent line plumes on the hot surface in steady turbulent RBC in water ($Pr = 5.09\text{--}5.24$) as well as in steady turbulent mixed convection (MC) in air ($Pr = 0.7$). We also include the spacings measured from the planforms of Gilpin *et al.* [17] for MC experiments in water ($Pr = 10.1$) and from the MC simulations of Pirozzoli *et al.* [15] at $Pr = 1$ to conduct the analysis over a two-decade range of Rayleigh numbers, $5.0 \times 10^7 \leq Ra_w \leq 2.17 \times 10^9$. The shear in our experiments is imposed externally in air, while in water, it is internally generated due to the large-scale flow to create about two orders of shear Reynolds numbers, $802 \leq Re \leq 15000$. We show that shear aligns the line plumes in the direction of the shear, with a mean spacing that increases with shear at the same Ra_w . An increase in Ra_w decreases the spacing at the same shear, with the spacings being a function of Pr also. This complex dependence of the mean spacings of line plumes on Ra_w , Re , and Pr is then shown to depend only on a shear parameter $S = U_{sh}^3 \alpha / g \beta \Delta T_w \nu^2$, which reflects the relative strength of shear with respect to buoyancy and dissipative effects, and a viscous shear length $Z_{sh} = \nu / U_{sh}$ for a given fluid.

II. EXPERIMENTS

A. Setup and procedure

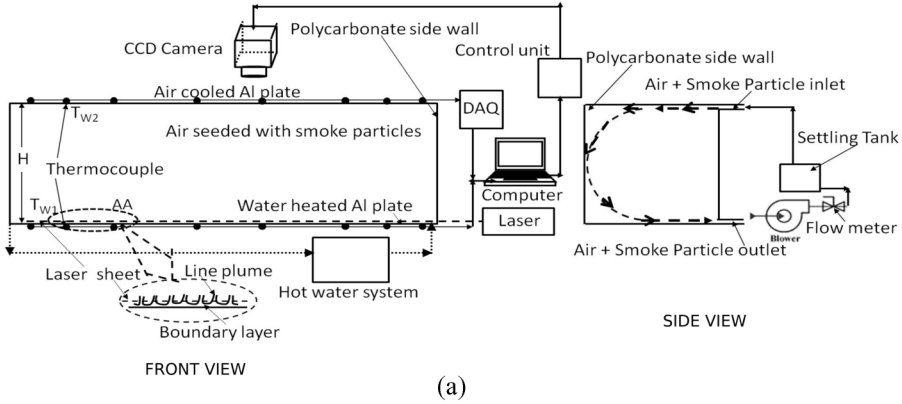
1. Mixed convection experiments with air

The schematic of the convection cell, which had an area of cross section $2.5 \text{ m} \times 0.5 \text{ m}$, used for the steady-state temperature-driven MC experiments in air at $Pr = 0.7$ with an imposed external flow is shown in Fig. 1(a). The top and the bottom aluminum plates were separated by four transparent polycarbonate side walls of height $H = 0.5 \text{ m}$. The bottom aluminum plate was maintained at a constant temperature using a temperature controlled water circulating system, while the top plate was air cooled by fans so that a constant mean temperature difference ΔT between the plates could be maintained. A flow of air was externally imposed in the convection cell through an inlet of height 25 mm at the top of one of the side walls and an outlet of height 15 mm at the bottom on the same side wall; the inlet and outlet extended over the entire length of the convection cell. The external flow was allowed to settle for nearly 60 minutes before taking the measurements.

ΔT was determined from spatial and temporal averaging of the plate temperatures recorded at 25 locations in each plate using PT100 resistance thermometers. The temperatures of the incoming and the outgoing air were measured using PT100 temperature sensors placed equidistantly over the entire length of the cell. The maximum possible error in temperature measurement was 0.25°C . External circulation flow rates ranging from $Q = 1087$ to 1736 lpm , at different ΔT maintained between the conducting plates, were used. These flow rates correspond to the mean shear velocities of air entering and leaving the convection cell over the range $0.29 \text{ m/s} \leq U_{sh} \leq 0.463 \text{ m/s}$ corresponding to a Reynolds number range of $9577 \leq Re \leq 15000$. The range of Rayleigh numbers in these experiments, $5.75 \times 10^7 < Ra_w < 1.55 \times 10^8$, was obtained by changing ΔT over the values shown in Table I.

2. RBC experiments with water

Steady turbulent RBC experiments in a water layer, confined between a hot copper plate at the bottom and a water-cooled glass plate at the top, were carried out in a glass tank of cross section $30 \text{ cm} \times 30 \text{ cm}$, with insulated side walls, in the setup shown in the Fig. 2. The bottom copper plate was maintained at a constant heat flux by a heater plate assembly connected to a variac. The heat flux was estimated from the measured temperature drop across a glass plate in the plate assembly by T-type thermocouples at three different locations. The temperatures of the hot Cu plate (T_h) and the cold glass plate (T_c) were measured at two different locations by T-type thermocouples, whose



(a)



(b)

FIG. 1. (a) Schematic of the setup for steady MC experiments in air at $Pr = 0.7$; (b) planform view of the plume structure obtained at $Ra_w = 1.55 \times 10^8$ and external flow rate $Q = 1736$ lpm with the dark line plumes marked with short, white linear segments for measurement of length. The image is of size $98.5 \text{ cm} \times 47.7 \text{ cm}$.

average was used to calculate the constant temperature difference of $\Delta T = T_h - T_c$. The error in temperature measurement was 0.02°C . Experiments were conducted over the range of Ra_w and Pr shown in Table I, obtained by changing the variac voltage, the layer height H , and the water flow rate over the cooling plate.

The velocity fields in a x - y plane at a height h_m , which was less than the Prandtl-Blasius boundary layer thickness (δ_{pb}) [22] and the natural convection boundary layer thickness (δ_{nc}) [5], were obtained by stereo particle image velocimetry (PIV). The flow was seeded with polyamide particles (mean diameter $d_p = 55 \mu\text{m}$ and density $\rho_p = 1.012 \text{ g cm}^{-3}$) and illuminated by a 1 mm thick horizontal laser sheet from a Nd:YAG laser (Litron, 100 mJ/pulse); the particles followed the flow since the Stokes number was less than 0.00415. The laser pulse separation was chosen so that the particle displacement was not more than one-fourth of the laser sheet thickness. Two Imager Pro HS cameras (LaVision GmbH, 1024×1280 pixels), oriented at 32.5° with the vertical, with a depth of field more than the laser sheet thickness, were used to capture the images at 15 Hz at the center of the hot plate. The imaging areas A_i , shown in Table II, were chosen so that a sufficient number of line plumes were present in A_i . Refraction errors were reduced by viewing the bottom plate through a water-filled prism placed over the top cold chamber, and the errors due to this oblique imaging were reduced by using a third-order polynomial mapping function obtained by imaging a calibration plate.

TABLE I. Experimental parameters, dimensionless numbers, and the plume spacings in the present study. \times , MC experiments by Gilpin *et al.* [17]; $*$, MC simulations by Pirozzoli *et al.* [15]. The value in parentheses indicates the power of 10 for Ra_w and Re.

Symbol	Type	Fluid	Pr	ΔT_w °C	H mm	Ra_w	Q lpm	U_{sh} mm/s	Re	λ mm
○	MC	Air	0.7	4.41	500	0.575 (8)	1087	290	9.577 (3)	49.3
						0.575 (8)	1167	311	10.28 (3)	56.2
						0.575 (8)	1249	333	10.997 (3)	64.9
□	MC	Air	0.7	7.95	500	1.01 (8)	1267	338	11.068 (3)	44.84
						1.01 (8)	1399	373	12.214 (3)	48.18
						1.01 (8)	1436	383	12.542 (3)	55.03
◇	MC	Air	0.7	9.88	500	1.24 (8)	1417	398	12.333 (3)	41.78
						1.24 (8)	1500	400	13.051 (3)	46.1
						1.24 (8)	1601	427	13.932 (3)	51.84
△	MC	Air	0.7	12.56	500	1.55 (8)	1537	410	13.283 (3)	40.11
						1.55 (8)	1676	447	14.482 (3)	43.33
						1.55 (8)	1736	463	15.0 (3)	47.93
●	RBC	Water	5.24	2.59	120	1.09 (8)		5.2	0.802 (3)	15.5
						1.09 (8)		5.4	0.832 (3)	15.6
						1.09 (8)		6.1	0.94 (3)	15.6
■	RBC	Water	5.18	3.27	150	2.79 (8)		8.8	1.717 (3)	15.4
						2.79 (8)		9.4	1.834 (3)	16.7
						2.79 (8)		10.0	1.951 (3)	15.8
◆	RBC	Water	5.09	4.58	175	6.03 (8)		10.8	2.49 (3)	17.2
						6.03 (8)		12.3	2.836 (3)	15.1
						6.03 (8)		13.4	3.09 (3)	16.3
×	MC	Water	10.1	11.5	457	21.7 (8)		29	9.573 (3)	23.84
*	MC	Simulations	1	5	855	0.5 (8)		261	10 (3)	131.3

A multipass adaptive window stereo cross correlation method (Davis) was applied on images obtained this way, after high-pass filtering, to calculate the 2D-3C vector field. The size of the interrogation window (D_I) and the particle concentrations were chosen so that the displacement of particles $x_p \leq D_I/4$ and at least 10 particles were present in an interrogation window at any time. Spurious vectors were removed by applying a median filter of $3 \text{ pix} \times 3 \text{ pix}$ neighborhood, and gaps were filled by interpolation. Other relevant parameters of the PIV measurements are shown in Table II, while two typical vector fields obtained at $Ra_w = 1.09 \times 10^8$ and 6.03×10^8 are shown in Fig. 3. Uncertainties in the estimated velocity in all the interrogation windows were calculated from the correlation statistics using the methodology of Wieneke [23], using the Davis software (LaVision GmbH). The maximum value of the mean uncertainty from all the images at the lowest and the highest Ra was 0.298 mm/s and 0.364 m/s, respectively. These mean uncertainties are 4.9% and 3.4% of the corresponding mean shear velocities at the corresponding Ra.

B. Detection of plumes

In MC experiments with air, the planforms of plume structures near the plate were made visible when a horizontal light sheet from a 532 nm Nd-Yag laser was scattered by the smoke particles injected into the external air flow circuit. The laser sheet was 2 mm thick with its centerline at $h_m = 4$ mm above the bottom hot plate. Since the plumes have a relatively lesser number of smoke particles, possibly since the smoke particles have to get into the plumes or into the boundary layers through entrainment from the bulk, they scatter less light and hence appear as dark lines in a bright background. Figure 1(b) shows the planform of plume structure visualized in this way above the

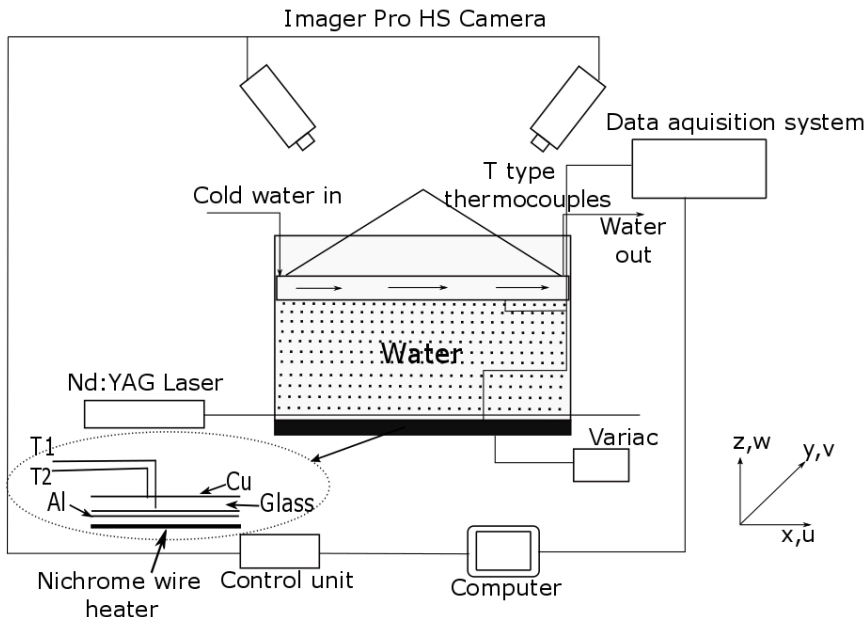


FIG. 2. Schematic of the setup for steady RBC experiments in water.

bottom horizontal plate at $Ra_w = 1.55 \times 10^8$. The thick darker lines in the image are the top view of the line plumes. The convection cell had a closed opaque top, and the top views of the plume structures near the bottom plate were hence captured through the side walls by a CCD camera at 10 fps. The perspective errors caused by this inclined camera axis were removed using a horizontal calibration plate in the plane of observation. Since all the plumes in the laser path will appear darker, no plumes are likely to be missed by this technique.

To detect plumes from the velocity fields obtained from PIV in the steady RBC experiments with water, we use the horizontal divergence criterion proposed by Vipin and Puthenveetil [24]. From the instantaneous horizontal divergence fields calculated from the horizontal velocity fields in a plane at height h_m , the criterion identifies regions with negative values as plumes. A $3 \text{ pix} \times 3 \text{ pix}$ smoothing mean filter was applied to the vector field to reduce the noise while calculating divergence. Figure 3 shows the horizontal divergence fields, overlaid over the horizontal vector fields at two Ra_w ; the colored, line-type regions show the plumes. We notice two types of regions in Figs. 3(a) and 3(b): (1) regions with smaller magnitudes of velocities where the line plumes are oriented in no particular direction and (2) regions with larger magnitudes of velocities where the line plumes are aligned in the direction of these larger velocity vectors. To study the effect of shear on plume spacings, we estimate the plume spacings only in the regions where the plumes are aligned and that have larger

 TABLE II. Parameters for the PIV measurements in water. Physical properties were estimated at $T_B = (T_h + T_c)/2$, the bulk fluid temperature.

Ra_w	T_B (°C)	h_m (mm)	δ_{pb} (mm)	δ_{nc} (mm)	A_i (mm ²)	Δt (s)	D_I (pix)	Overlap (%)	Spatial resolution (mm)
1.09×10^8	31.42	1.5	11.1	2.2	83.08×71.94	0.0667	32	50	1.04
2.79×10^8	31.88	1.0	8.9	2.0	82.28×70.38	0.0667	32	50	1.03
6.03×10^8	32.60	1.3	7.5	1.8	84.10×73.86	0.0667	32	50	1.05

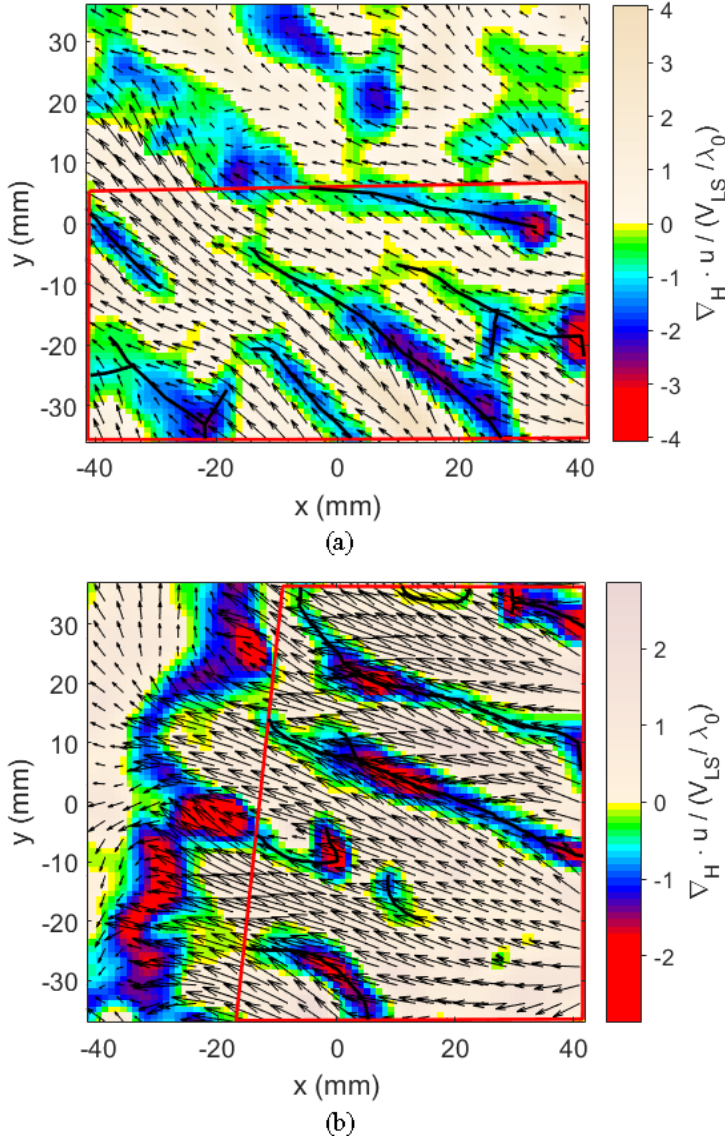


FIG. 3. Dimensionless horizontal divergence fields $[\nabla_H \cdot u / (V_{LS} / \lambda_0)]$, overlaid over the horizontal velocity vector fields, in a horizontal plane at a height h_m from the hot surface in RBC in water. (a) $Ra_w = 1.09 \times 10^8$, $Re = 832$, and $h_m = 1.5$ mm; (b) $Ra_w = 6.03 \times 10^8$, $Re = 2490$, and $h_m = 1.3$ mm. Plumes are the colored regions. Shear dominant areas are shown by the red polygon. L_p is measured by adding up the length of the black lines in the plume regions in the shear-dominant regions. The large-scale flow velocity V_{LS} is estimated from the Reynolds number based on V_{LS} given by $Re_{LS} = V_{LS}H/\nu = 0.55Ra_w^{4/9}Pr^{-2/3}$ [16].

magnitudes of horizontal velocity. We estimate the average magnitude of horizontal velocity in such regions, shown by the red polygons in Fig. 3, and use this as the mean shear velocity U_{sh} .

We also measure the plume spacings from Gilpin *et al.* [17] and Pirozzoli *et al.* [15]. Plumes in Gilpin *et al.* [17] were visualized by the phenolphthaleine-based electrochemical technique [25]. The technique causes color changes to the dye only close to the hot surface, and the dye with a different color than the bulk near the hot plate then gets drawn into the plumes, thereby making

them visible. In the case of Pirozzoli *et al.* [15], plumes are identified as the regions with positive temperature fluctuations (T') from their given T' fields in a horizontal plane close to the hot surface, which we estimate to be at 12.2 mm from the hot plate for a chosen ΔT_w of 5 °C.

C. Measurement of plume spacing

Once the plumes are detected as described above, the mean plume spacing λ at each Ra_w and Re were estimated from the images by measuring the total plume length L_p in an area A and then using

$$\lambda = A/L_p, \quad (5)$$

given in Ref. [5]. The plume lengths were measured from images similar to that in Figs. 1(b) and 3 by using a program that covers the line plumes with short linear segments on mouse clicks over the line plumes, which then calculates the total length of these segments to give L_p . Figure 1(b) shows a planform in air at $\text{Ra}_w = 1.55 \times 10^8$ and 1736 lpm external flow, with the line plumes covered with such short linear segments, the sum of whose lengths give L_p . Similarly, Fig. 3 shows two plan forms in water at $\text{Ra}_w = 1.09 \times 10^8$ and 6.03×10^8 , where the plumes are covered by line segments.

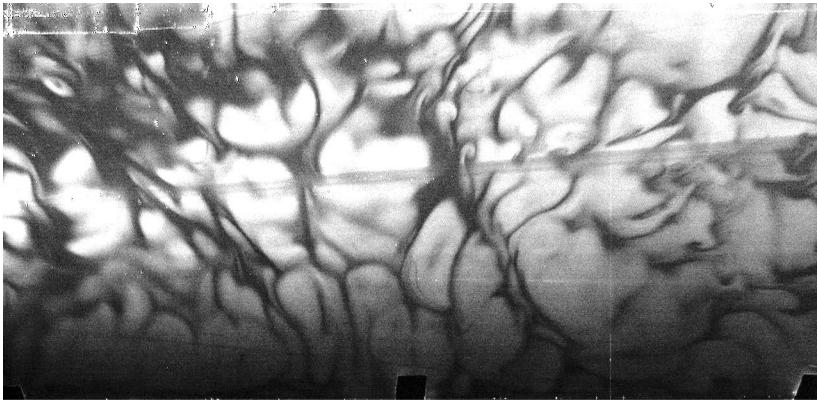
A possible error of 1.5% in λ was estimated from multiple measurements from the same planform in air. Similarly, for planforms in water, a 3% error in λ was estimated by measuring the maximum and minimum possible values of L_p from planforms. To estimate the error in the estimate of λ from Pirozzoli *et al.* [15], we estimate L_p from subregions in their Fig. 4(f) by marking segments in the red regions alone that show the highest values of T' , and then in the red and yellow regions that show slightly lower values of T' . This process is repeated for different subregions to get a range of L_p , and the error in λ is estimated from this range; the maximum possible error in λ was 2.9%. The error in the estimate of λ from Gilpin *et al.* [17] was obtained by making multiple measurements of L_p from different subregions of the planform given in their Fig. 4(c) to give a maximum possible error of 4.3%. These values of errors in λ , or the errors derived using these values, are shown in the subsequent plots as the vertical error bars.

III. ANALYSIS OF MEAN PLUME SPACINGS

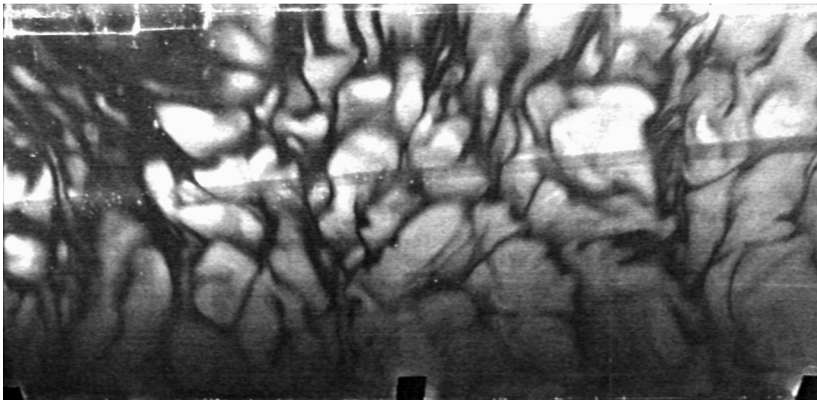
A. Qualitative analysis

Figure 4 shows the planforms in mixed convection in air at $\text{Ra}_w = 1.55 \times 10^8$ at Re of 13 283, 14 482, and 15 000. The direction of external shear is from top to bottom in these figures. The planforms show that with increase in shear the plumes are distributed more uniformly, with the plumes becoming more aligned in the direction of shear. It also appears that the mean plume spacing increases in Fig. 4(c) compared to that in Fig. 4(a). Similar increased uniformity of spacing, increased alignment in shear direction, and larger mean plume spacing with increasing shear were also observed in the planforms in air at the other Ra_w shown in Table I. Since the spacing between the plumes is directly proportional to the distance over which the boundary layer between the plumes develop, before becoming unstable, it is hence clear that shear changes the stability of the local boundary layers between the plumes in turbulent convection. Figure 5 shows the planforms of plume structure at approximately the same Re of 10 997 and 11 068 but at different Ra_w of 5.75×10^7 and 1.01×10^8 . It is clear that the density of plumes increases with increase in Ra_w resulting in smaller plume spacings with increase in Ra_w .

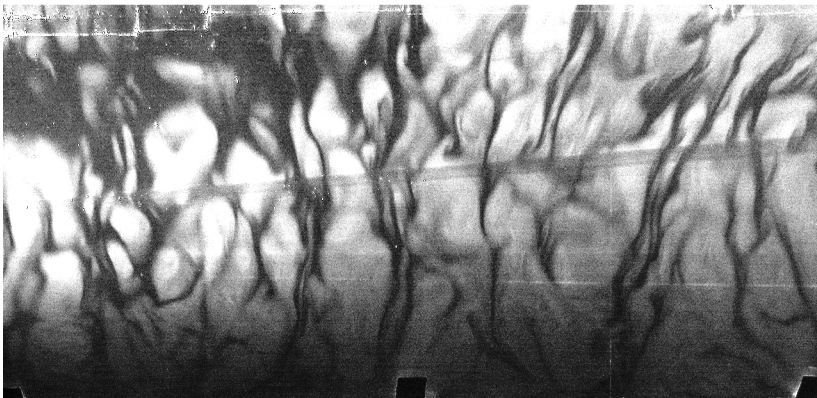
The plume structure at the center of the bottom hot plate in steady RBC in water at $\text{Ra}_w = 1.09 \times 10^8$ and 6.03×10^8 is shown in Fig. 3. Unlike in the case of MC planforms in Figs. 4(a) to 4(c), where the effect of shear is seen to approximately align the plumes over the whole of the planform, here we notice that there are regions that show alignment of plumes, which are marked by the red polygon, while there are also regions in which the plumes are oriented randomly. The aligned plumes occur in regions with higher horizontal velocity magnitudes, as could be noticed by the larger velocity vectors in these regions in Figs. 3(a) and 3(b). As seen in Table I, Re based on



(a)



(b)



(c)

FIG. 4. Planforms of plume structure in MC in air at $Ra_w = 1.55 \times 10^8$. (a) $Re = 13.28 \times 10^3$; (b) $Re = 14.48 \times 10^3$; (c) $Re = 15 \times 10^3$. Flow is from top to bottom. The images are of size $98.5 \text{ cm} \times 47.7 \text{ cm}$.

the average shear velocity U_{sh} in these regions are an order lower than the corresponding Re in Figs. 4(a) to 4(c). The shear is lower in the case of RBC experiments in water since it is created by the self-generated large-scale flow, at a higher Pr than in air, whereas the shear in experiments with air is externally forced. Such a lower shear in the water experiments could be the reason for the splitting

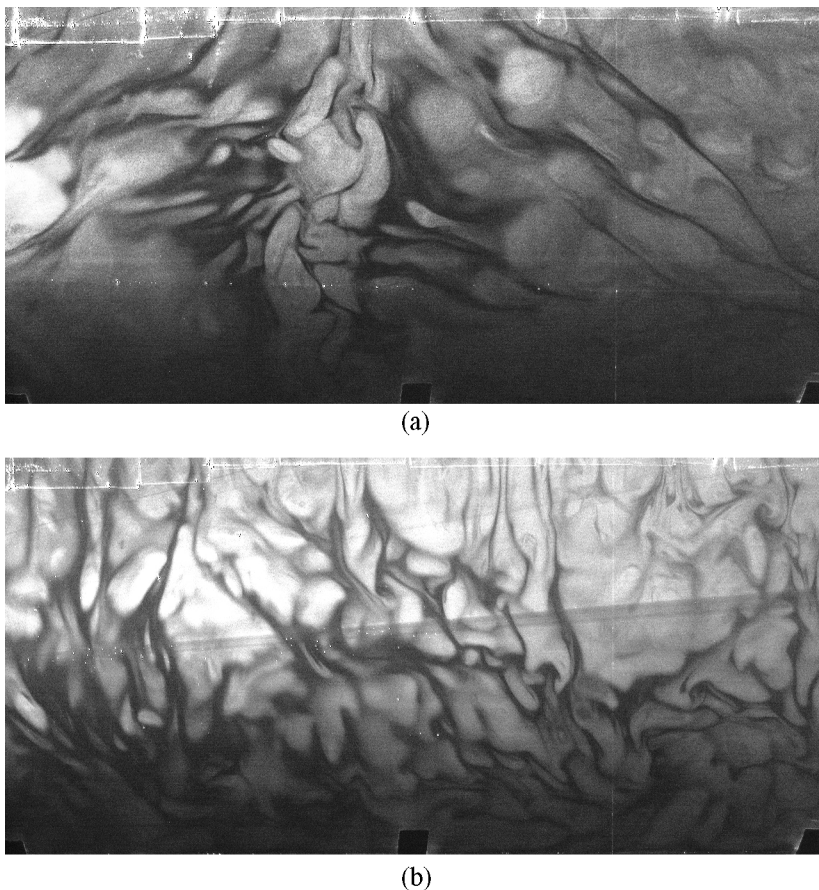


FIG. 5. Planforms of plume structure at approximately the same Re at two different Ra_w in MC in air. (a) $Re = 9.58 \times 10^3$ at $Ra_w = 5.75 \times 10^7$; (b) $Re = 9.6 \times 10^3$ at $Ra_w = 1.55 \times 10^8$. Flow is from top to bottom. The images are of size $98.5 \text{ cm} \times 47.7 \text{ cm}$.

of the planforms into shear-dominant and shear-free regions in Fig. 3. In corroboration with this observation, we also observe that the extent of regions with aligned plumes increases with increase in Ra_w in these RBC experiments, since the large-scale flow strength increases with increase in Ra_w . Since the planforms in Fig. 3 are over an area of 60 cm^2 while those in Fig. 4 are over an area of 4700 cm^2 the density of plumes are much more at the same Ra_w in water compared to that in air; an increase in Pr hence seems to decrease the mean plume spacing. Unlike in the case of planforms in air in Fig. 4, an increase of plume spacing in the shear-dominant regions, or an increase in plume density with increase in Ra_w is not clearly seen in the planforms in water in Fig. 3.

B. Quantitative analysis of plume spacings

Figure 6 shows the variation of the mean plume spacing λ as a function of the shear velocity U_{sh} at different Ra_w in water and air. The hollow symbols show the variation of λ in air, while the filled symbols show it in water. The same type of symbols indicates the same Ra_w . The solid line in the figure shows λ_0 for the no-shear case at $Pr = 0.7$, evaluated using (1) at $Ra_w = 1.55 \times 10^8$, i.e., at the same Ra_w as Δ . The dashed line shows λ_0 at $Pr = 5.09$ and $Ra_w = 6.03 \times 10^8$, corresponding to \blacklozenge . The figure also shows the values of λ measured from Gilpin *et al.* [17] at $Pr = 10.1$ and from

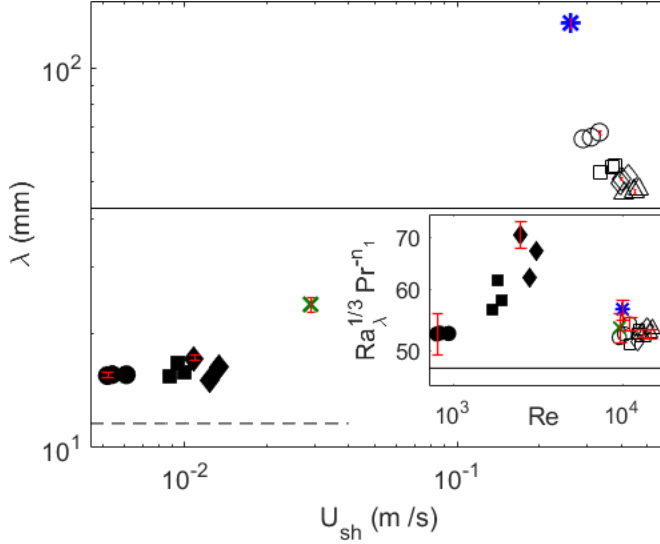


FIG. 6. Variation of the mean plume spacing with the shear velocity. Hollow symbols indicate MC experiments in air at $Pr = 0.7$ for the following Ra_w : \circ , $Ra_w = 5.75 \times 10^7$; \square , $Ra_w = 1.01 \times 10^8$; \diamond , $Ra_w = 1.24 \times 10^8$; \triangle , $Ra_w = 1.55 \times 10^8$. Filled symbols indicate RBC experiments in water for the following Ra_w and Pr : \bullet , $Ra_w = 1.09 \times 10^8$, $Pr = 5.24$; \blacksquare , $Ra_w = 2.79 \times 10^8$, $Pr = 5.18$; \blacklozenge , $Ra_w = 6.03 \times 10^8$, $Pr = 5.09$. \times , MC experiments by Gilpin *et al.* [17] in water at $Pr = 10.1$ and $Ra_w = 2.17 \times 10^9$; $*$, MC simulations by Pirozzoli *et al.* [15] at $Pr = 1$ and $Ra_w = 5 \times 10^7$; -----, λ_0 given by (1) for $Ra_w = 6.03 \times 10^8$ and $Pr = 5.09$; —, λ_0 given by (1) for $Ra_w = 1.55 \times 10^8$ and $Pr = 0.7$. The inset shows the variation of the dimensionless plume spacing with Reynolds number; —, $Ra_{\lambda_0}^{1/3} Pr^{-n_1} = 47.5$ (3).

Pirozzoli *et al.* [15] at $Pr = 1$. The error bars show the error in λ at some of the U_{sh} , estimated as discussed in Sec. II C.

The most noticeable feature of the figure is that the values of λ in air are about 4 to 5 times that in water, even though both are at around the same order of Ra_w , possibly because of the higher shear in air, which are about an order larger than that in water. Compared to the values in the no-shear case, shown by the solid and the dashed lines in Fig. 6, shear increases the plume spacing to higher values; this increase from the no-shear values being lower in the lower Pr case. The low Pr data shows that at any Ra_w , shown by any of the hollow symbols in Fig. 6, shear increases λ . Further, the curves of each hollow symbol move down with increase in Ra_w , implying that an increase in Ra_w at around similar shear at low Pr strongly decreases λ . Similar trends are also shown by the higher Pr data, but the increase of λ with shear seems to be much smaller here, possibly since the values of shear itself are small. Further, the increase of shear in these RBC experiments is accompanied by an increase of Ra_w also, since the large-scale flow strength scales as $Ra_w^{4/9}$ [4], which, as we saw above, has the effect of reducing the spacings. The decrease of λ with Ra_w , seen in the low Pr case cannot be seen for water, possibly since this decrease is offset by the increase in λ due to shear. The spacing in Pirozzoli *et al.* [15], at similar U_{sh} as that in air, seems to be disproportionately higher than those in air, since Ra_w is only slightly lower and Pr slightly higher in this case compared to air. In the case of Gilpin *et al.* [17], Ra_w is an order larger than those in water, which should have reduced λ compared to those in water. The observed contrary behavior could be due to the increase of U_{sh} , and possibly Pr .

The above trends can be seen better in the variation of the dimensionless plume spacing $\lambda/(Z_w Pr^{n_1}) = Ra_{\lambda}^{1/3}/Pr^{n_1}$ with the dimensionless shear velocity, Re , shown in the inset in Fig. 6. The error bars in the figure show the estimated error in $Ra_{\lambda}^{1/3} Pr^{-n_1}$, calculated using the errors in

ΔT_w and λ . For the case of no shear, as per (1), $\text{Ra}_{\lambda_0}^{1/3}/\text{Pr}^{\eta_1} = 47.5$, which is shown as the solid line in the inset. The increase of plume spacing with shear at any Ra_w and Pr , seen in the main figure, is seen as the increase of $\text{Ra}_{\lambda}^{1/3}$ with Re at any Pr . This increase seems to have the same trend at all Ra_w , even though this dependence does not seem to be any simple power law. The decrease in λ with Ra_w at the same shear, observed in the main figure, is also seen in the inset figure in air, where the values of $\text{Ra}_{\lambda}^{1/3}$ move down with increase in Ra_w at the same shear.

The variation of λ with Pr , seen in the inset, seems involved. The vertical offset of the water data from the solid line is much more than that in the case of air, even when the shear velocity is much smaller in water; the effect of shear to increase λ over its no-shear value λ_0 is seen to be much more in water compared to that in air. Noting that the air data are at much lower Pr compared to that of the water data, shear seems to increase the mean plume spacing much more at higher Pr than at lower Pr . However, contrary to this trend, an increase in Pr seems to reduce the increase in λ with shear for the data of Gilpin *et al.* [17]. The data of Ref. [17] at $\text{Pr} = 10.1$, are at a much higher Re than our water data but still do not show as much increase of λ over the corresponding no-shear values as shown by the water data. The data of Gilpin *et al.* [17], which is at almost the same Re as our air data at lowest Re but with Ra_w two order larger, show an equal vertical offset from their no-shear values as in the case of air; the reduction in λ with increase in Ra_w seem to be less at higher Pr . To complicate matters, the data of Pirozzoli *et al.* [15], which is at almost the same Ra_w and Re as our air data but at slightly higher Pr , show an increase of λ compared to that in air; the Pr dependence of λ does not seem to be monotonic. Clearly, the variation of λ with shear shows quite a complex dependence on Re , Ra_w and Pr ; we now present a scaling analysis which accounts for this nontrivial dependence.

C. Scaling of mean plume spacing with shear

1. Stability condition

Castaing *et al.* [26] showed that in the presence of shear, the gravitational instability of natural convection boundary layers gets modified to result in a critical boundary layer thickness, given by

$$\text{Ra}_{\delta} = A + B\text{Re}_{\delta}^2, \quad (6)$$

where $\text{Ra}_{\delta} = g\beta\Delta T_w\delta^3/\nu\alpha$ is the critical Rayleigh number based on the critical thermal boundary layer thickness δ at which the boundary layer becomes unstable. $\text{Re}_{\delta} = U_{\text{sh}}\delta/\nu$ is the critical Reynolds number based on δ , with $A(\text{Pr})$ and $B(\text{Pr})$ being unknown functions of Prandtl number. We define $\tilde{\delta} = \delta/Z_w$ and a shear parameter

$$S = \frac{U_{\text{sh}}^3\alpha}{g\beta\Delta T_w\nu^2} = \frac{1}{\text{Ra}_{\text{sh}}} = \frac{\text{Re}^3}{\text{Ra}_w} = \left(\frac{Z_w}{Z_{\text{sh}}}\right)^3, \quad (7)$$

which indicates the relative strength of shear with respect to buoyancy and dissipative effects, where the Rayleigh number,

$$\text{Ra}_{\text{sh}} = \frac{g\beta\Delta T_w Z_{\text{sh}}^3}{\nu\alpha}, \quad (8)$$

is based on the viscous-shear length,

$$Z_{\text{sh}} = \frac{\nu}{U_{\text{sh}}}. \quad (9)$$

Equation (6) can now be rewritten in terms of $\tilde{\delta}$ and S as

$$\tilde{\delta}^3 - BS^{2/3}\tilde{\delta}^2 - A = 0. \quad (10)$$

Solving (10), we obtain the only real root for $\tilde{\delta}$ as

$$\tilde{\delta} = \frac{b}{3} + \frac{2^{1/3} b^2}{3 \zeta} + \frac{2^{-1/3}}{3} \zeta, \quad (11)$$

where

$$\zeta = 27A + 2b^3 + 3\sqrt{3}\sqrt{27A^2 + 4Ab^3} \text{ with} \quad (12)$$

$$b = BS^{2/3}. \quad (13)$$

Equation (11) can now be expanded in a series about $b = 0$ as

$$\tilde{\delta} = A^{1/3} + \frac{b}{3} + \frac{b^2}{9A^{1/3}} + O(b^3) \text{ terms.} \quad (14)$$

Rewriting (14) in terms of λ and using (13), we obtain

$$\frac{\delta}{\lambda} = \left(\frac{A}{\text{Ra}_\lambda}\right)^{1/3} + \frac{B}{3} \left(\frac{S^2}{\text{Ra}_\lambda}\right)^{1/3} + \frac{B^2}{9A^{1/3}} \left(\frac{S^4}{\text{Ra}_\lambda}\right)^{1/3} + O(S^2) \text{ terms.} \quad (15)$$

We now assume that

$$\delta/\lambda = C\text{Pr}^n \quad (16)$$

for small shear. This assumption implies that δ and λ have the same functional dependence on Ra_w and Re so that their ratio becomes only a function of Pr . Such is the case for plume spacings with no shear, as has been shown in Ref. [5], where both λ and δ scale as $C_i Z_w \text{Pr}^{n_i}$, with different values of C_i and n_i for λ and δ , so that their ratio scale as $C\text{Pr}^n$. We expect the same to occur in the presence of small shear; as we show later, this assumption accounts for the variation of λ in the present range of shear. Using (16) in (15) and neglecting terms with power of S greater than one, which is again valid for small shear, we obtain

$$\left(\frac{A}{\text{Ra}_\lambda}\right)^{1/3} + \frac{B}{3} \left(\frac{S^2}{\text{Ra}_\lambda}\right)^{1/3} = C\text{Pr}^n. \quad (17)$$

For $S \rightarrow 0$, i.e., with no shear, $\lambda \rightarrow \lambda_0$ and $\text{Ra}_\lambda \rightarrow \text{Ra}_{\lambda_0}$, for which (17) should tend to the corresponding no-shear relation (3), which implies that

$$A = C^3 \text{Pr}^{3n} \text{Ra}_{\lambda_0}. \quad (18)$$

2. Scaling of excess plume spacings with shear

Substituting (18) in (17), and rearranging, we obtain the difference of the plume spacing in the presence of shear from its no-shear value, $\lambda^* = \lambda - \lambda_0$, normalized by the viscous-shear length Z_{sh} (8), to scale as

$$\frac{\lambda^*}{Z_{\text{sh}}} = \frac{S}{D}, \quad (19)$$

where $D(\text{Pr}) = 3C\text{Pr}^n/B$. Figure 7 shows the variation of $D\lambda^*/Z_{\text{sh}}$ with S in our experiments in air and water as well as for those measured from Refs. [15,17]. The error bars show the estimated error in $D\lambda^*/Z_{\text{sh}}$ and in S at some of the values of S , calculated from the possible errors in ΔT_w , λ , and U_{sh} discussed in Sec. II. The complex dependence of λ on Ra_w , Re , and Pr , seen in Fig. 6, now collapses on to a common, simple, linear dependence of $D\lambda^*/Z_{\text{sh}}$ on S , in agreement with (19), when we use the variation

$$D = 52.7\text{Pr}^{-2.8}, \quad (20)$$

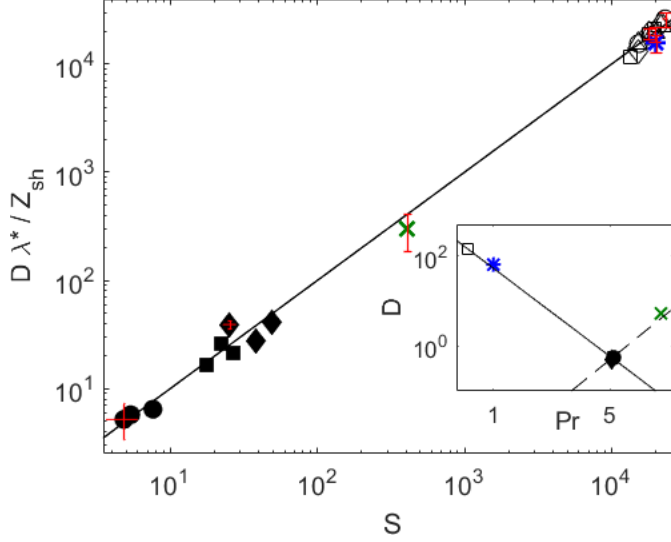


FIG. 7. Variation of λ^* , the difference between the mean plume spacing with shear (λ) and without shear (λ_0) normalized by the viscous-shear length Z_{sh} (8), with the dimensionless shear parameter S (7); The symbols are as per Fig. 6 and Table I; —, (19). The inset shows the variation of the prefactor D in (19) with Pr ; —, (20); ----, (21).

for $Pr < 5$, and

$$D = 0.004Pr^3, \quad (21)$$

for $Pr > 5$, shown in the inset. The increasing and the decreasing strong power law dependences of λ^* on Pr , for $Pr < 5$ and $Pr > 5$ respectively, could be because the thermal and velocity boundary layers cross over at $Pr \sim 1$.

The relation (19) can also be rewritten as

$$\frac{\lambda^*}{H} = \frac{1}{D} \frac{Re^2}{Ra_w}, \quad (22)$$

showing that λ^* scales as Re^2 and as $1/Ra_w$. Analogous to (3) for the case of no shear, (19) can also be rewritten in terms of Rayleigh and Reynold's numbers based on λ^* as

$$\frac{Ra_{\lambda^*}}{Re_{\lambda^*}^2} = \frac{1}{D}. \quad (23)$$

3. Scaling of ratio of plume spacings

The ratio of mean plume spacing with shear to that without shear λ/λ_0 can be obtained from (19) to scale as

$$\frac{\lambda}{\lambda_0} = 1 + ES^{2/3}, \quad (24)$$

where

$$E(Pr) = \frac{1}{DC_1Pr^{m_1}}. \quad (25)$$

Figure 8 shows the variation of $(\lambda/\lambda_0 - 1)/E$ with the shear parameter S , using the values of E calculated using (20), (21), and (25). The solid line shows the variation predicted by (24) while the

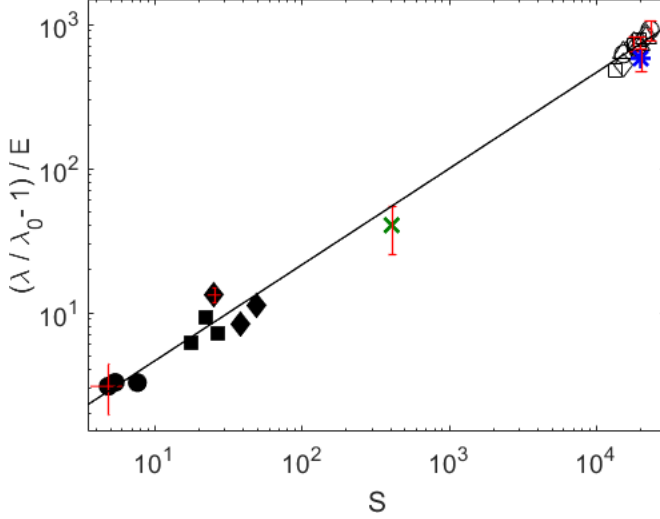


FIG. 8. Variation of the ratio of the mean plume spacing with shear (λ) and that without shear (λ_0) with the dimensionless shear parameter S (7). The symbols are as per Fig. 6 and Table 1; —, (24).

error bars at some of the S show the estimated errors in $(\lambda/\lambda_0 - 1)/E$ and S , calculated from the possible errors in ΔT_w , λ , and U_{sh} . The figure shows that the ratios of plume spacings with and without shear over the range of Ra_w , Re , and Pr in our study obey the relation (24). Using (7), (20), and (21) in (24), we obtain

$$\frac{\lambda}{\lambda_0} = 1 + 4 \times 10^{-4} Pr^{2.7} \left(\frac{Re}{Ra_w^{1/3}} \right)^2, \quad \text{for } Pr < 5 \quad (26)$$

and

$$\frac{\lambda}{\lambda_0} = 1 + 5.36 Pr^{-3.1} \left(\frac{Re}{Ra_w^{1/3}} \right)^2, \quad \text{for } Pr > 5. \quad (27)$$

Expressions (26) and (27) show that λ/λ_0 , the ratio of plume spacings at all Pr scale as $(Re/Ra_w^{1/3})^2$, but the spacings increase with Pr for $Pr < 5$ while they decrease with Pr for $Pr > 5$, presumably due to the crossover of the thermal and velocity boundary layers at $Pr \sim 1$.

4. Scaling of length of plumes with shear

Since $L_p = A/\lambda$ from (5), the above relations for λ also result in expressions for the total length of plumes on the surface in the presence of shear, analogous to the relations for the plume lengths L_{p0} in the absence of shear, given by Puthenveetil *et al.* [5]. The left-hand side of (19), after dividing by λ , can be rewritten as L_p^*/L_{p0} , where $L_p^* = L_{p0} - L_p$ is the reduction in plume length with shear from the no-shear values. Using (24) to replace the λ on the right-hand side gives the results that the ratio of the reduction in plume length with shear to the plume length in the absence of shear is given by

$$\frac{L_p^*}{L_{p0}} = \frac{ES^{2/3}}{1 + ES^{2/3}}. \quad (28)$$

Similarly, since $\lambda/\lambda_0 = L_{p0}/L_p$ in (24), the ratio of plume lengths with shear to that without shear is

$$\frac{L_p}{L_{p0}} = \frac{1}{1 + ES^{2/3}}. \quad (29)$$

5. Upper limit of the present analysis

If we continue the above analysis without dropping the last term of order $S^{4/3}$ in (15), we obtain

$$\frac{\lambda}{\lambda_0} = 1 + ES^{2/3} + E^2S^{4/3}. \quad (30)$$

The present scaling laws is then valid when the last term in (30) is small compared to the previous term, i.e., when

$$S < \frac{1}{E^{3/2}}. \quad (31)$$

Using the values of E from (25), with D given by (20) and (21) we obtain the upper limits of the present scaling laws as $S < 5.31 \times 10^5$ for $\text{Pr} = 0.7$, $S < 1.25 \times 10^5$ for $\text{Pr} = 1$, $S < 184$ for $\text{Pr} = 5.24$, and $S < 3.87 \times 10^3$ for $\text{Pr} = 10.1$. All these limits are above the range of the present data for the corresponding Pr .

IV. DISCUSSION AND CONCLUSIONS

The primary contribution of the present work is the scaling of mean plume spacing (λ) on the hot surface in turbulent Rayleigh-Bénard convection (RBC) in the presence of internally generated shear, as well as in mixed convection (MC), where the shear is externally supplied. The difference of λ with the corresponding mean plume spacing in the absence of shear (λ_0), $\lambda^* = \lambda - \lambda_0$ is shown to scale as $\lambda^* = SZ_{\text{sh}}/D$ (19), where $S = \text{Re}^3/\text{Ra}_w$ is a dimensionless shear parameter that shows the relative strength of shear with respect to buoyancy and dissipative effects (7), Z_{sh} the viscous shear length (9), and D a function of Pr [(20) and (21)]. Such a scaling implies that $\lambda^* = Z_w^3/(Z_{\text{sh}}^2 D)$, a function of two length scales near the plate, namely, Z_w , the buoyancy-dissipative length scale (2) and Z_{sh} .

The above scaling also means that, analogous to the relation $\text{Ra}_{\lambda_0}^{1/3} = 47.5\text{Pr}^{0.1}$ for plume spacing without shear (3), the plume spacings in the presence of shear are given by $\text{Ra}_{\lambda^*}/\text{Re}_{\lambda^*}^2 = 0.02\text{Pr}^{2.8}$ for $\text{Pr} < 5$ and by $\text{Ra}_{\lambda^*}/\text{Re}_{\lambda^*}^2 = 250\text{Pr}^{-3}$ for $\text{Pr} > 5$, (23), where the subscript λ^* indicates that the dimensionless numbers are based on λ^* . We expect the positive and negative exponents of Pr in these relations for $\text{Pr} < 5$ and $\text{Pr} > 5$ to occur because the thermal and velocity boundary layers cross over at $\text{Pr} \sim 1$. The dimensionless excess plume spacing in the presence of shear then scales as $\lambda^*/H \sim \text{Re}^2/(D\text{Ra}_w)$ (22). These relations, when written in terms of the ratio of plume spacings in the presence of shear with those with no shear, imply that $\lambda/\lambda_0 \sim \text{Pr}^{2.7}(\text{Re}/\text{Ra}_w^{1/3})^2$ for $\text{Pr} < 5$ (26) and as $\lambda/\lambda_0 \sim \text{Pr}^{-3.1}(\text{Re}/\text{Ra}_w^{1/3})^2$ for $\text{Pr} > 5$ (27). All of these relations for λ also give rise to corresponding relations (28) and (29) for the length of plumes L_p that form on hot surfaces in RBC and MC.

These scalings of the plume spacings with shear were obtained by measuring the mean plume spacing from two types of experiments, as well as from two earlier studies by Gilpin *et al.* [17] and Pirozzoli *et al.* [15]. Visualizations of the plume structure on the hot plate in steady, turbulent, MC in air, which was forced externally by a shear, gave λ at $\text{Pr} = 0.7$. Plumes detected from PIV vector fields, using the horizontal divergence criterion [24], from the shear-dominant regions in steady, turbulent RBC in water, gave λ at $5.09 < \text{Pr} < 5.24$. Measurements of λ from these two experiments, along with those from Refs. [15,17], provided the variation of λ over one order of Ra_w and Re over $0.7 < \text{Pr} < 10.1$, to enable us to obtain the above scaling of the plume spacings. These experiments showed that shear makes the line plumes aligned along the shear direction with λ

increasing with shear for a given fluid and Ra_w . Correspondingly, for a given fluid at the same Re , an increase in Ra_w reduced the spacing. In addition, the spacings also had a nonmonotonic dependence on Pr . These complex dependencies of the mean plume spacings in turbulent convection with shear on Ra_w , Re , and Pr were successfully captured by the above discussed scaling laws.

The above scaling laws, were obtained from the instability condition given by Castaing *et al.* [26] for natural convection boundary layers forced by shear, using the assumption that the ratio of critical boundary layer thickness and the plume spacing is only a function of Pr , after neglecting terms in the stability condition that had a power of S greater than one. The proposed scaling laws for the spacings are hence likely to hold only for small shear, given by upper limits of S , for each Pr ; these limits were found to be $S = 184$ for $Pr = 5.24$ and $S = 5.31 \times 10^5$ for $Pr = 0.7$. At larger shear, forced convection effects would become predominant, with the flux scaling showing the standard relations for forced convection [13]. The evolution of the spacings beyond the present range of shear towards the forced convection limit needs to be investigated.

-
- [1] O. Shishkina and C. Wagner, Local fluxes in turbulent Rayleigh-Bénard convection, *Phys. Fluids* **19**, 085107 (2007).
 - [2] L. Pera and B. Gebhart, On the stability of natural convection boundary layer flow over horizontal and slightly inclined surfaces, *Int. J. Heat Mass Transfer* **16**, 1147 (1973).
 - [3] T. Haramina and A. Tilgner, Coherent structures in boundary layers of Rayleigh-Bénard convection, *Phys. Rev. E* **69**, 056306 (2004).
 - [4] B. A. Puthenveetil and J. H. Arakeri, Plume structure in high Rayleigh number convection, *J. Fluid Mech.* **542**, 217 (2005).
 - [5] B. A. Puthenveetil, G. S. Gunasegarane, Y. K. Agrawal, D. Schmeling, J. Bosbach, and J. H. Arakeri, Length of near-wall plumes in turbulent convection, *J. Fluid Mech.* **685**, 335 (2011).
 - [6] S. A. Theerthan and J. H. Arakeri, Planform structure and heat transfer in turbulent free convection over horizontal surfaces, *Phys. Fluids* **12**, 884 (2000).
 - [7] S. A. Theerthan and J. H. Arakeri, A model for near wall dynamics in turbulent Rayleigh-Bénard convection, *J. Fluid Mech.* **373**, 221 (1998).
 - [8] J. Bosbach, S. Weiss, and G. Ahlers, Plume Fragmentation by Bulk Interactions in Turbulent Rayleigh-Bénard Convection, *Phys. Rev. Lett.* **108**, 054501 (2012).
 - [9] S. Grossman and D. Lohse, Scaling in thermal convection: A unifying theory, *J. Fluid Mech.* **407**, 27 (2000).
 - [10] N. Shi, M. S. Emran, and J. Schumacher, Boundary layer structure in turbulent Rayleigh-Bénard convection, *J. Fluid Mech.* **706**, 5 (2012).
 - [11] M. van Reeuwijk, H. J. J. Jonker, and K. Hanjalić, Wind and boundary layers in Rayleigh-Bénard convection. II. Boundary layer character and scaling, *Phys. Rev. E* **77**, 036312 (2008).
 - [12] X. Wang, An experimental study of mixed, forced, and free convection heat transfer from a horizontal flat plate to air, *J. Heat Transfer* **104**, 139 (1982).
 - [13] F. Incropera, A. Knox, and J. Maughan, Mixed-convection flow and heat transfer in the entry region of a horizontal rectangular duct, *J. Heat Transfer* **109**, 434 (1987).
 - [14] H. Imura, R. Gilpin, and K. Cheng, An experimental investigation of heat transfer and buoyancy induced transition from laminar forced convection to turbulent free convection over a horizontal isothermally heated plate, *J. Heat Transfer* **100**, 429 (1978).
 - [15] S. Pirozzoli, M. Bernardini, R. Verzicco, and P. Orlandi, Mixed convection in turbulent channels with unstable stratification, *J. Fluid Mech.* **821**, 482 (2017).
 - [16] G. S. Gunasegarane and B. A. Puthenveetil, Dynamics of line plumes on horizontal surfaces in turbulent convection, *J. Fluid Mech.* **749**, 37 (2014).
 - [17] R. R. Gilpin, H. Imura, and K. C. Cheng, Experiments on the onset of longitudinal vortices in horizontal Blasius flow heated from below, *J. Heat Transfer* **100**, 71 (1978).

- [18] A. Garai, J. Kleissl, and S. Sarkar, Flow and heat transfer in convectively unstable turbulent channel flow with solid-wall heat conduction, *J. Fluid Mech.* **757**, 57 (2014).
- [19] R. J. Adrian, Hairpin vortex organization in wall turbulence, *Phys. Fluids* **19**, 041301 (2007).
- [20] S. Lyons, T. Hanratty, and J. McLaughlin, Turbulence-producing eddies in the viscous wall region, *AIChE J.* **35**, 1962 (1989).
- [21] R. Falco, A coherent structure model of the turbulent boundary layer and its ability to predict Reynolds number dependence, *Phil. Trans. R. Soc. Lond. A* **336**, 103 (1991).
- [22] G. Ahlers, S. Grossmann, and D. Lohse, Heat transfer and large-scale dynamics in turbulent Rayleigh-Bénard convection, *Rev. Mod. Phys.* **81**, 503 (2009).
- [23] B. Wieneke, PIV uncertainty quantification from correlation statistics, *Meas. Sci. Technol.* **26**, 074002 (2015).
- [24] K. Vipin and B. A. Puthenveetil, Identification of coherent structures on the horizontal plate in turbulent convection, in *Proceeding of the 8th World Conference on Experimental Heat Transfer, Fluid Mechanics and Thermodynamics, June 16–20, 2013, Lisbon, Portugal* (2013).
- [25] E. Sparrow and R. Husar, Longitudinal vortices in natural convection flow on inclined plates, *J. Fluid Mech.* **37**, 251 (1969).
- [26] B. Castaing, G. Gunaratne, F. Heslot, L. Kadanoff, A. Libchaber, S. Thomae, X.-Z. Wu, S. Zaleski, and G. Zanetti, Scaling of hard thermal turbulence in Rayleigh-Bénard convection, *J. Fluid Mech.* **204**, 1 (1989).